Shape Factor and Hydraulic Conductance in Noncircular Capillaries: I. One-Phase Creeping Flow

December 14, 2000

T. W. Patzek[1] and D. B. Silin[2]

Accepted by J. Colloid and Interface Science

Short title: Shape Factor and Hydraulic Conductance - I

[1] The corresponding author: Department of Civil and Environmental Engineering, 591 Evans Hall, University of California, Berkeley, CA 94720, email: patzek@patzek.berkeley.edu, Tel: 510-643-5834.

[2] Lawrence Berkeley National Laboratory, silin@patzek.berkeley.edu.

Abstract

In Part I of this paper, we use the Mason-Morrow shape factor, i.e., a dimensionless hydraulic radius, and corner half-angles to capture the geometry of noncircular capillaries pertinent to a physically adequate pore network description of porous media. We give analytic expressions for random corner half angles that satisfy a given shape factor calculated from the microscopic images of pore space. We demonstrate that use of the shape factor leads to particularly simple expressions for the hydraulic conductance in single-phase flow through noncircular capillaries. In particular, we obtain the hydraulic conductances of arbitrary triangular ducts semi-analytically, using conformal mapping. The conductances of equilateral triangular, rectangular and elliptic ducts are calculated analytically. In Part II (1), we use the capillary shape factor to derive universal expressions for the hydraulic conductance in two-phase flow with no slip and perfect slip boundary conditions at the water corner filament-oil interfaces.

Keywords: Noncircular capillary; shape factor; pore network; hydraulic conductance; one phase flow; conformal mapping

1 Introduction

Pore space of a rock is a disordered 3D network of *angular* pore bodies (sites or nodes) connected by angular pore throats (bonds or links), cf. e.g. (2). The hydraulic resistance to flow is mostly in the links. The pore throat radii are usually distributed over 2-4 orders of magnitude. Resistance to laminar flow varies as the fourth power of the smallest throat radius and hydraulic resistance to single fluid flow is distributed over 8-16 orders of magnitude. When two or more immiscible fluids occupy the rock, the hydraulic resistances of corner water filaments, **Figure 1**, and intermediate oil filaments may span well over 20 orders of magnitude. In cases when the local hydraulic resistances are distributed over more than 4-5 orders of magnitude (3), transport is percolative, i.e., spatially heterogeneous and repeatable, rather than diffusive.

At microscopic scale, capillary forces dominate, e.g., (2, 4). Hence, quasi-static pore network models of drainage and imbibition that fully account for capillarity can predict absolute permeability, capillary pressures and relative permeabilities in many rocks at core scale (5-8). In fact, pore-network predictions of absolute permeability of Fontainebleau sandstone agreed with experiment over five orders of magnitude (7). Pore networks based on the three-dimensional models of rock formation and transformation processes have been especially successful in such predictions (6, 7), (8). It is therefore important to have an efficient and reliable procedure that (1) characterizes the pore angularity; (2) predicts the hydraulic conductance of angular pores in single-phase flow; and (3) predicts the hydraulic conductance of angular pores in two-phase flow with

arbitrary contact angles and with a no-slip or perfect slip boundary condition at the corner filament-bulk fluid interfaces.

This paper is organized as follows. First, we choose the Mason and Morrow shape factor to characterize the angular pores and demonstrate why this is a good choice. Second, we characterize the single-phase hydraulic conductance of noncircular capillaries in terms of this shape factor. In Part II of the paper, we perform highly accurate finite element calculations and correlate the two-phase hydraulic conductance of wetting liquid in angular capillaries in terms of the corner filament shape factor, corner half-angle and contact angle.

2 Pore geometry

Real pore bodies and pore throats have complex and variable cross-sections. Often they are approximated as cylindrical ducts (noncircular capillaries) of constant but arbitrary cross-section. This means that the idealized pores are translationally symmetric along the cylinder generators, **Figure 2**.

In pore network models, the average pore cross-sections are commonly approximated by triangles of arbitrary shape, rectangles and ellipses, **Figure 3**. The first two cross-sections will render the simplest polygonal tubes with three and four corners. This idealization is sufficient to capture the essential geometry of real pores and the essential physics of corner flow. We do not consider here the extremely narrow slit-like pores, which should be treated as fractures.

As shown so elegantly by Hwang, (9), if we know the hydraulic radius of a capillary with an arbitrary cross-section, $R_h = A/\mathrm{P}$, where A is the cross sectional area and P is the

perimeter, we can compute the mean curvature and the capillary rise. We can also use the hydraulic radius to vastly simplify the derivation of the Mayer-Stowe-Princen theory (10-13) of threshold capillary pressure for invasion of an angular capillary. As we shall demonstrate here, the capillary shape factor is its hydraulic radius made dimensionless by division through the perimeter.

2.1 Triangular pores

We shall begin by describing the triangular capillary geometry with three independent parameters: the corner half-angles, β_1, β_2 and $\beta_3 = \pi/2 - \beta_1 - \beta_2$, and the shape factor *G*, which can be thought of as a *dimensionless hydraulic radius* of the capillary. We adopt a convention that $0 \le \beta_1 \le \beta_2 \le \beta_3 \le \pi/2$, so that β_1 and β_2 are the two corner half angles subtended at the longest side of the triangle (its base). The pore cross-sectional area *A* and its perimeter P can be expressed through Mason and Morrow's (14) "shape factor" defined by equation

$$G = \frac{A}{\mathrm{P}^2} = \frac{R_h}{\mathrm{P}} \qquad [1]$$

and the radius of the inscribed circle *r*. The pore area is

$$A = \frac{1}{2}\mathrm{P}r \text{, or } r = \frac{2A}{\mathrm{P}} \qquad [2]$$

because the cross-section is composed of six triangles of equal heights *r*, cf. **Figure 4**.

If the radius of the inscribed circle is normalized with respect to the perimeter then

$$\frac{r}{\mathrm{P}} = \frac{2A}{\mathrm{P}^2} = 2G \text{ or } r^2 = 4GA = 4Gr^2 \sum_{i=1}^{3} \cot \beta_i \,. \qquad [3]$$

Hence, since $\beta_3 = \pi/2 - \beta_1 - \beta_2$,

$$G = \frac{1}{4\sum_{i=1}^{3} \cot \beta_i} = \frac{1}{4} \tan \beta_1 \tan \beta_2 \cot(\beta_1 + \beta_2) \,. \qquad [4]$$

The maximum possible value of G, $G_{\max} = \sqrt{3}/36 \approx 0.048113$, corresponds to equilateral triangles with $\beta_1 = \beta_2 = \pi/6$. The minimum possible value of G, $G_{\min} = 0$, corresponds to slit-like pores. In **Appendix A**, we demonstrate that for any admissible value of the shape factor G, $0 \le G \le G_{\max}$, there exist two extreme angles of β_2: $\beta_{2,\min}(G)$ and $\beta_{2,\max}(G)$, beyond which Eq. [4] has no solution, see Figure 5. More specifically, we assert the following. Inasmuch as the shape factor depends only on the angles of the triangle, all possible triangles can be parameterized through all triples $(\beta_1, \beta_2, \beta_3)$ of nonnegative numbers whose sum equals $\pi/2$. This parameterization becomes a one-to-one (up to a similarity) mapping if we consider only the triples sorted in the increasing order: $0 \le \beta_1 \le \beta_2 \le \beta_3 \le \pi/2$. Given a shape factor G, $0 \le G \le G_{\max}$, there exists an ordered triple $(\beta_1, \beta_2, \beta_3)$ of the half-angles of a triangle satisfying Eq. [4] if and only if $\beta_{2,\min}(G) \le \beta_2 \le \beta_{2,\max}(G)$, where $\beta_{2,\min}(G)$ and $\beta_{2,\max}(G)$ are calculated in Appendix A. Thus, for an admissible shape factor *G*, a triple of corner half angles may be chosen at random as follows, **Figure 6 - Figure 7**:

(1) Find the bounds on β_2, $\beta_{2,\min} \le \beta_2 \le \beta_{2,\max}$ from Eqs. [A.16] and [A.17].

(2) Pick at random a value of $\beta_{2,\min} \le \beta_2 \le \beta_{2,\max}$

(3) Use Eq. [A.3] to calculate the appropriate value of β_1

(4) Calculate $\beta_3 = \pi/2 - \beta_1 - \beta_2$.

2.2 Rectangular and elliptic ducts

For ducts with square cross-sections, all four half-angles are equal to $\pi/4$ and $G = 1/16$. Circular ducts have no corners and $G = 1/4\pi$. For simplicity, all ducts with shape factors between those of equilateral triangle and square can be mapped onto squares, and those with shape factors above 1/16 onto circles.

3 Single-phase creeping flow in capillary ducts

3.1 Problem Statement

We shall consider the steady state, creeping isothermal flow of a Newtonian, incompressible and constant viscosity fluid. With these assumptions, the continuity equation and the Navier-Stokes equation combine to produce the elliptic Poisson equation:

$$\nabla^2 \vec{v} = \frac{1}{\mu}\left(\nabla p - \rho \vec{f}\right) \qquad [5]$$

where $\vec{v}$ is the fluid velocity; $\vec{f}$ is the body force per unit mass; μ is the fluid viscosity; and ρ is its density.

We choose a Cartesian coordinate system with the x_3-axis parallel to the axis of the duct. We assume that within the fluid there exists a constant pressure gradient, $\partial p / \partial x_3 = -(p_0 - p_L)/L = -\Delta p / L$, in the decreasing x_3-direction. This pressure gradient generates a rectilinear flow field along the duct. We thus seek a solution to the following hydrodynamic problem:

$$\begin{aligned} &\nabla^2 v + \frac{\Xi}{\mu} = 0 \\ &\Xi = \left(\frac{\Delta p}{L} + \rho f_3 \right) \\ &v(x_1, x_2) = 0 \ \text{ on } \ \Gamma_s \end{aligned} \qquad [6]$$

where Δp is the pressure drop in the duct, L is the duct length, $v(x_1, x_2)$ vanishes at the duct wall Γ_s, f_3 is a constant, and Ξ is minus the average gradient of the total driving force per unit area.

The solution of Eq. [6] allows one to relate the volumetric flow rate in the duct to gradient of the driving force:

$$Q = \langle v \rangle A = -\mathcal{g}(\nabla p - \rho f_3) = \mathcal{g}\Xi \qquad [7]$$

where $\langle v \rangle$ is the average flow velocity and $\mathcal{g}$ is the hydraulic conductance of the duct, i.e., the volumetric flow rate per unit pressure gradient. By analogy with the well-known Hagen-Poiseuille formula for cylindrical tubes, we express the flow conductance as

$$\mathcal{g} = \frac{r^2 A}{\chi \mu} \qquad [8]$$

where r is the inscribed circle radius, A is the flow area, and χ is the dimensionless flow resistance factor,

$$\chi = \frac{r^2 \Xi}{\langle v \rangle \mu}. \qquad [9]$$

3.1 Hydraulic conductance of triangular ducts

Let us consider a rectilinear duct with equilateral triangle as its cross section, **Figure 8**.

If we place the origin at the intersection of the medians and let the negative x_1-axis pass through one vertex, e.g., (15), the equation of an equilateral triangle with altitude $3a$ becomes

$$(x_1 - a)(x_1 - \sqrt{3}x_2 + 2a)(x_1 + \sqrt{3}x_2 + 2a) = 0 \qquad [10]$$

Since $\nabla^2 (x_1 - a)(x_1 - \sqrt{3}x_2 + 2a)(x_1 + \sqrt{3}x_2 + 2a) = 12a$, then

$$v = \left(\frac{\Xi a^2}{12\mu} \right) (1 - x_1/a)(x_1/a - \sqrt{3}x_2/a + 2)(x_1/a + \sqrt{3}x_2/a + 2) \qquad [11]$$

The total flow rate through the duct is obtained by integrating velocity [11] over the cross-section

$$Q = \int_{x_1=-2a}^{x_1=a} \int_{x_2=-\frac{x_1+2a}{\sqrt{3}}}^{x_2=\frac{x_1+2a}{\sqrt{3}}} v(x_1, x_2) dy dx = \frac{9\sqrt{3}}{20} \frac{a^4}{\mu} \Xi \qquad [12]$$

The duct cross-sectional area is $A = 3\sqrt{3}a^2$, hence the mean velocity and volumetric flow rate are

$$\begin{aligned} \langle v \rangle &= \frac{Q}{A} = \frac{3}{20}\frac{a^2}{\mu}\Xi = \frac{1}{20\sqrt{3}}\frac{A}{\mu}\Xi, \\ Q &= \mathcal{G}_{\max}\Xi = \frac{1}{20\sqrt{3}}\frac{A^2}{\mu}\Xi = \frac{3}{5}\frac{A^2 G_{\max}}{\mu}\Xi, \end{aligned} \qquad [13]$$

where $G_{\max} = \sqrt{3}/36$ is the equilateral triangle shape factor. Thus, the dimensionless hydraulic conductance of the equilateral triangle duct is

$$\tilde{\mathcal{G}}_{\max} = \frac{\mathcal{G}_{\max}\mu}{A^2} = \frac{3}{5}G_{\max} \qquad [14]$$

For an arbitrary triangular duct, we shall solve the boundary problem [6], integrate the fluid velocity over the duct cross-section and apply Eq. [13] to calculate the hydraulic conductance as a function of the triangle shape factor. The highly accurate conformal mapping solution is described in **Appendix B** and the results are shown in **Figure 9**.

Figure 9 shows that the diagonal line with the slope of 3/5 approximates the dimensionless hydraulic conductance of an arbitrary triangular cross-section duct characterized by an arbitrary shape factor *G*. Thus, we assert that

$$\tilde{\mathcal{G}} = \frac{\mathcal{G}\mu}{A^2} \approx \frac{3}{5}G \qquad [15]$$

for any triangle. According to this assertion, the dimensionless conductance of a triangular duct is a straight line when plotted versus the shape factor *G*, **Figure 10**.

3.2 Hydraulic conductance of rectangular ducts

If the rectangle has sides 2a and 2b, and if we choose the orientation of the coordinates system such as in **Figure 11**, then the solution of Problem [6] is (15):

$$v(x_1,x_2)=\frac{\Xi}{2\mu}\left[b^2-x_2^2+\frac{32b^2}{\pi^3}\sum_{n=0}^{\infty}\frac{(-1)^{n+1}\cosh[(2n+1)\pi x_1/2b]\cos[(2n+1)\pi x_2/2b]}{(2n+1)^3\cosh[(2n+1)\pi a/2b]}\right] \quad [16]$$

The average velocity and the hydraulic conductance are:

$$\begin{aligned}\langle v\rangle &= \frac{A\Xi}{4\mu\varepsilon}\left[\frac{1}{3}-\frac{64}{\varepsilon\pi^5}\sum_{n=0}^{\infty}\frac{\tanh[(2n+1)\pi\varepsilon/2]}{(2n+1)^5}\right]\\ \tilde{g} &= \left(1+\frac{1}{\varepsilon}\right)^2\left[\frac{1}{3}-\frac{64}{\varepsilon\pi^5}\sum_{n=0}^{\infty}\frac{\tanh[(2n+1)\pi\varepsilon/2]}{(2n+1)^5}\right]G,\quad \varepsilon=a/b\end{aligned} \quad [17]$$

For a square duct, Eq. [17] reduces to

$$\begin{aligned}\langle v\rangle &= \frac{A\Xi}{\mu}\left[\frac{1}{12}-\frac{16}{\pi^5}\sum_{n=0}^{\infty}\frac{\tanh[(2n+1)\pi/2]}{(2n+1)^5}\right]\\ \tilde{g} &= \left[\frac{1}{12}-\frac{16}{\pi^5}\sum_{n=0}^{\infty}\frac{\tanh[(2n+1)\pi/2]}{(2n+1)^5}\right]16G=0.5623G\end{aligned} \quad [18]$$

The dimensionless hydraulic conductance in rectangular cross-section ducts is plotted in Figure 10 versus the shape factor.

3.3 Hydraulic conductance of elliptic ducts

For an elliptical cross-section duct, **Figure 12**, the shape factor is:

$$G=\frac{\pi}{16}\frac{\varepsilon}{E^2\left(\sqrt{1-\varepsilon^2}\right)},\quad \varepsilon=b/a \quad [19]$$

where $E(e)$ is the elliptic integral of the second kind, defined as

$$E(e) = \int_0^1 \sqrt{\frac{1-e^2t^2}{1-t^2}}dt = \int_0^{\pi/2} \sqrt{1-e\sin^2 t}\,dt\,, \qquad [20]$$

where

$$e \equiv \frac{c}{a} = \frac{\sqrt{a^2-b^2}}{a} = \sqrt{1-\varepsilon^2} \qquad [21]$$

is the ellipse eccentricity. For a circle, $e = 0$, $E(0) = \pi/2$, and $G = 1/(4\pi)$.

The dimensionless hydraulic conductance of an elliptical duct is

$$\tilde{\boldsymbol{g}} = \frac{1}{4\pi}\frac{\varepsilon}{1+\varepsilon^2} = \frac{4}{\pi^2}\frac{E^2(\sqrt{1-\varepsilon^2})}{1+\varepsilon^2}G \qquad [22]$$

If one approximates the circumference of the ellipse as

$$P \approx 2\pi\sqrt{\frac{a^2+b^2}{2}} \qquad [23]$$

then

$$G = \frac{A}{\mathrm{P}^2} \approx \frac{\pi ab}{2\pi^2(a^2+b^2)} = \frac{1}{2\pi}\frac{\varepsilon}{1+\varepsilon^2}\,, \qquad [24]$$

and Eq. [22] can be approximated as

$$\tilde{\boldsymbol{g}} \approx \frac{1}{2}G\,. \qquad [25]$$

Expression [23] approximates the exact ellipse circumference to within 11 percent. For the circular cross-section duct, of course, the well-known (16) result is exact equality in Eq. [25].

The shape factors and the dimensionless conductances may be scaled from zero to one by division through the respective end-point values. The rescaled conductances may then be fit with polynomials, **Figure 13**.

Rectangle: $\tilde{g} = 0.3214\tilde{G}^3 + 0.0630\tilde{G}^2 + 0.6109\tilde{G}$, where $\tilde{G} = \frac{G}{G_{max}} = 16G$ and

$$\tilde{g} = \frac{\tilde{g}}{\tilde{g}_{max}} = \frac{\tilde{g}}{0.5623/16} \qquad [26]$$

Ellipse: $\tilde{g} = 0.1366\tilde{G}^3 + 0.0556\tilde{G}^2 + 0.8077\tilde{G}$, where $\tilde{G} = \frac{G}{G_{max}} = 4\pi G$ and

$$\tilde{g} = \frac{\tilde{g}}{\tilde{g}_{max}} = \frac{\tilde{g}}{1/(8\pi)} \qquad [27]$$

4 Conclusions

1. The geometric significance of the Mason and Morrow shape factor has been elucidated for the triangular cross-section capillaries and an analytic algorithm for calculating the admissible capillary shapes, given the shape factor, has been described.
2. The shape factor plays an important role in obtaining the semi-analytical or analytical expressions for the hydraulic conductances of noncircular capillaries filled with a single fluid.

3. In particular, the dimensionless hydraulic conductances of triangular, rectangular and elliptic ducts filled with a single fluid are simple power functions of the shape factor.

Appendix A: Admissible shape factor and half-angles

To investigate the solvability of Eq. [4], let us rewrite it in the following equivalent form

$$G = \frac{1}{4}\tan\beta_2\left(1 - \frac{2}{1 + \dfrac{\sin\left(2\beta_1 + \beta_2\right)}{\sin\beta_2}}\right) \qquad [A.1]$$

Since $\beta_1 \le \beta_2 \le \beta_3$ and $\beta_1 + \beta_2 + \beta_3 = \dfrac{\pi}{2}$ we infer that

$$0 \le \beta_1 \le \frac{\pi}{6} \quad \text{and} \quad \beta_1 \le \beta_2 \le \frac{\pi}{4} - \frac{\beta_1}{2} \qquad [A.2]$$

Equation [A.1] (and, therefore, Eq. [4]) can be solved with respect to β_1 explicitly:

$$\beta_1 = -\frac{1}{2}\beta_2 + \frac{1}{2}\arcsin\left(\frac{\tan\beta_2 + 4G}{\tan\beta_2 - 4G}\sin\beta_2\right) \qquad [A.3]$$

From Eq. [A.2] and with $\beta_3 = \dfrac{\pi}{2} - \left(\beta_1 + \beta_2\right)$ we immediately obtain that

$$\frac{\pi}{4} - \frac{\beta_1}{2} \le \beta_3 \le \frac{\pi}{2} - \beta_1 \qquad [A.4]$$

Comparing Eqs. [A.2] and [A.4] we automatically get $\beta_2 \le \beta_3$, therefore, all three the half angles are ordered in the ascending order. Hence, both $0 \le \beta_1 \le \beta_2 \le \beta_3$ and $\beta_1 + \beta_2 + \beta_3 = \frac{\pi}{2}$ hold true simultaneously if and only if the inequalities [A.2] hold true. Inequalities [A.2] can be equivalently rewritten in the following form:

$$0 \le \beta_2 \le \frac{\pi}{4} \quad \text{and} \quad 0 \le \beta_1 \le \begin{cases} \beta_2, & \text{if } 0 \le \beta_2 \le \frac{\pi}{6} \\ \frac{\pi}{2} - 2\beta_2, & \text{if } \frac{\pi}{6} < \beta_2 \le \frac{\pi}{4} \end{cases} \qquad \text{[A.5]}$$

Now, if we fix the half angle β_2, unconstrained maximum of the right-hand side of Eq. [A.1] with respect to β_1 is attained at $\beta_1 = \frac{\pi}{4} - \frac{\beta_2}{2}$. As β_1 increases from 0 to this value, the right-hand side of Eq. [A.1] (and of Eq. [4]) also increases monotonically. However, the angle β_1 is restricted by inequalities [A.5] and a straightforward calculation demonstrates that the inequality $\beta_2 \le \frac{\pi}{4} - \frac{\beta_2}{2}$ holds true if $0 \le \beta_2 \le \frac{\pi}{6}$, and $\frac{\pi}{2} - 2\beta_2 \le \frac{\pi}{4} - \frac{\beta_2}{2}$ hold true if $\frac{\pi}{6} < \beta_2 \le \frac{\pi}{4}$. Therefore, the constrained maximum of the right-hand side of Eq. [A.1] with respect to β_1 is attained at

$$\beta_1(\beta_2) = \begin{cases} \beta_2, & \text{if } 0 \le \beta_2 \le \frac{\pi}{6} \\ \frac{\pi}{2} - 2\beta_2, & \text{if } \frac{\pi}{6} < \beta_2 \le \frac{\pi}{4} \end{cases} \qquad \text{[A.6]}$$

Obviously, from $\beta_1 = \frac{\pi}{2} - 2\beta_2$ it follows that $\beta_2 = \beta_3$. Since permutation of the angles in a triangle does not affect its shape factor, we can flip β_1 with β_3 when $\frac{\pi}{6} < \beta_2 \le \frac{\pi}{4}$. Such a transformation simplifies Eq. [A.6] into

$$\beta_1(\beta_2) = \beta_2, \quad 0 \le \beta_2 \le \frac{\pi}{4} \qquad [A.7]$$

Therefore, in order to plot all admissible shape factors versus β_2 we just need to substitute Eq. [A.7] into Eq. [A.1]:

$$G_{\max}(\beta_2) = \frac{1}{4}\tan\beta_2 \left(1 - \frac{2}{1 + \frac{\sin(3\beta_2)}{\sin\beta_2}} \right), \qquad 0 \le \beta_2 \le \frac{\pi}{4}. \qquad [A.8]$$

Using standard trigonometric identities, we reduce [A.8] to

$$G_{\max}(\beta_2) = \frac{-\tan^3\beta_2 + \tan\beta_2}{8} \qquad [A.9]$$

The plot of the function defined by Eq. [A.9] gives us the shape of the dome in **Figure 5**. To find the limits $\beta_{2,\min}$ and $\beta_{2,\max}$ for a given admissible shape factor *G*, we need to investigate the solution to the cubic equation

$$t^3 - t + 8G = 0 \qquad [A.10]$$

with *G* between 0 and $G_{\max} = \sqrt{3}/36$. Since $t = \tan(\beta_2)$ and β_2 varies between 0 and $\pi/4$, we are looking only for the solutions to [A.10] that are between 0 and 1. If $G = 0$,

Eq. [A.10] has two roots fulfilling this condition $t = 0$ and $t = 1$ (see **Figure 14a**) that corresponds to $\beta_2 = 0$ and $\beta_2 = \frac{\pi}{4}$. When $G = G_{\max} = \sqrt{3}/36$, Eq. [A.10] admits only one double root $t = 1/\sqrt{3}$ in the interval $[0,1]$ (respectively, $\beta_2 = \frac{\pi}{6}$, an equilateral triangle), **Figure 14c**. In an intermediate case, where $0 < G < \sqrt{3}/36$ (**Figure 14b**), we obtain two roots $0 < t_{\min} < t_{\max} < 1$. Therefore, we obtain

$$\beta_{2,\min} = \arctan\left(\mathrm{t}_{\min}\right) \quad \text{and} \qquad \beta_{2,\max} = \arctan\left(\mathrm{t}_{\max}\right) \tag{A.11}$$

To calculate $t_{\min}$ and $t_{\max}$ analytically, we apply the Cardano formulae. We obtain for all the roots of Eq. [A.10]

$$t_{1,2,3} = \frac{2}{\sqrt{3}} \operatorname{Re} \sqrt[3]{-12\sqrt{3}G + i\sqrt{1 - 432G^2}} \tag{A.12}$$

where i is the imaginary unit. To select the two nonnegative solutions out of the three given by Eq. [A.12], we apply the following argument. Clearly, all solutions are represented by

$$t_\nu = \frac{2}{\sqrt{3}} \cos\left(\frac{\varphi_\nu}{3}\right), \quad \text{where} \quad \varphi_\nu = \arccos\left(-12\sqrt{3}G\right) + 2\pi\left(\nu - 1\right) \quad \text{and} \quad \nu = 1,2,3 \tag{A.13}$$

Moreover, Eq. [A.13] implies that $\frac{\pi}{2} \le \varphi_1 \le \pi$. Hence $\frac{\pi}{6} \le \frac{\varphi_1}{3} \le \frac{\pi}{3}$ and the roots [A.12] are located as shown in **Figure 15.** Hence,

$$t_{\min} = t_3 = \frac{2}{\sqrt{3}} \cos\left(\frac{\arccos\left(-12\sqrt{3}G\right)}{3} + \frac{4\pi}{3} \right) \qquad [A.14]$$

$$t_{\max} = t_1 = \frac{2}{\sqrt{3}} \cos\left(\frac{\arccos\left(-12\sqrt{3}G\right)}{3} \right) \qquad [A.15]$$

Thus, finally we obtain:

$$\beta_{2,\min} = \arctan\left(\frac{2}{\sqrt{3}} \cos\left(\frac{\arccos\left(-12\sqrt{3}G\right)}{3} + \frac{4\pi}{3} \right) \right) \qquad [A.16]$$

and

$$\beta_{2,\max} = \arctan\left(\frac{2}{\sqrt{3}} \cos\left(\frac{\arccos\left(-12\sqrt{3}G\right)}{3} \right) \right) \qquad [A.17]$$

Appendix B: Solution of a triangular duct flow problem using conformal mapping

The boundary-value problem [6] for a Poisson equation in a triangle can be solved semi-analytically using conformal mapping techniques, see (17). To do this, we need to complete three steps. First, a conformal mapping of the unit disk onto the triangular domain where we are solving the boundary-value problems should be constructed. Second, we need to impose boundary conditions in such a way that we obtain a Dirichlet

problem for a Laplace equation, which is equivalent to the original problem. We then calculate the image of the boundary conditions on the unit circle where the conformal mapping is applied. In the unit disk the solution to the Laplace equation is calculated from Poisson's integral. In the third step, the solution in the original domain is obtained from the solution on the unit disk with the conformal mapping constructed above, and, finally the solution to the original Poisson equation [6] is calculated. In this appendix, we describe in more detail how this procedure works in our case.

A conformal mapping of a unit disk onto a triangle with the angles $2\beta_1$, $2\beta_2$ and $2\beta_3$ Figure 4 is given by

$$w = S(z) = C_1 \int_{z_0}^{z} (\zeta - \zeta_1)^{\alpha_1} (\zeta - \zeta_2)^{\alpha_2} (\zeta - \zeta_3)^{\alpha_3} \, d\zeta + C_2 \qquad \text{[B.1]}$$

Here C_1 and C_2 are complex coefficients which define rotation, dilation and shift in the plane *w*, the exponents α_i are determined by the angles of the triangle $\alpha_i = \frac{\beta_i}{\pi} - 1$, and ζ_i are arbitrary complex numbers whose modules are equal to one, $i = 1, 2, 3$. The complex number z_0 also can be chosen arbitrarily inside the unit disk. The arbitrariness, however, assumes that the coefficients C_1 and C_2 have to be recalculated as a different set of parameters ζ_i and z_0 is selected. The choice of the parameters ζ_i also determines the point onto which the center of the disk is mapped.

Numerical algorithms for computing the parameters for the transformation defined by Eq. [B.1] have been developed recently (18) and are available both in Fortran and in MATLAB[3] versions, (19, 20).

To apply transformation [B.1], we need to slightly modify the boundary-value problem [6]. For this purpose we will look for the solution to Eq. [6] in the form

$$v\left(x_1, x_2\right) = v_0\left(x_1, x_2\right) + u\left(x_1, x_2\right), \qquad \text{[B.2]}$$

where $v_0\left(x_1, x_2\right)$ is a function satisfying the Poisson equation, but probably violating the boundary conditions, whereas the function $u\left(x_1, x_2\right)$ satisfies Laplace equation with some boundary conditions in such a way that the sum [B.2] is the solution to [6]. There is certain arbitrariness in the choice of $v_0\left(x_1, x_2\right)$, but for simplicity we put

$$v_0\left(x_1, x_2\right) = -\frac{\Xi}{4\mu}\left(x_1 + x_2\right)^2 \qquad \text{[B.3]}$$

Then, for the function $u\left(x_1, x_2\right)$ we obtain the following boundary-value problem:

$$\begin{aligned} \nabla^2 u\left(x_1, x_2\right) &= 0, \\ u\left(x_1, x_2\right)\big|_{\Gamma} &= \frac{\Xi}{4\mu}\left(x_1 + x_2\right)^2 . \end{aligned} \qquad \text{[B.4]}$$

If we introduce a complex variable $w = x_1 + x_2 i$, then from [B.1]

$$\varphi\left(\eta_1, \eta_2\right) = u\left(\operatorname{Re} S\left(z\right), \operatorname{Im} S\left(z\right)\right), \qquad \text{[B.5]}$$

[3] MATLAB is a registered trademark of MathWorks, Inc.

where $z = \eta_1 + \eta_2 i$, is a harmonic function defined on the unit disk. A conformal transformation [B.1] maps the unit circle onto the boundary of the triangle Γ, therefore the boundary condition for the function φ is:

$$\varphi(\eta_1, \eta_2)\big|_{\eta_1^2+\eta_2^2=1} = \frac{\Xi}{4\mu}\left(\mathrm{Re}\, S(\eta_1 + i\eta_2) + \mathrm{Im}\, S(\eta_1 + i\eta_2)\right)^2 \qquad [B.6]$$

The solution to Laplace equation with the boundary condition defined by Eq. [B.6] is furnished by the Poisson integral (17):

$$\varphi(\eta_1, \eta_2) = \frac{1}{2\pi}\int_{-\pi}^{\pi} \frac{\Xi}{4\mu}\left|S(z(\alpha))\right|^2 \frac{1-\rho^2}{\rho^2 - 2\rho\cos(\alpha-\psi)+1}\, d\alpha, \qquad [B.7]$$

where $\left|S(z(\alpha))\right|^2 = \left(\mathrm{Re}\, S(\cos\alpha + i\sin\alpha) + \mathrm{Im}\, S(\cos\alpha + i\sin\alpha)\right)^2$, $\rho = \left(\eta_1^2 + \eta_2^2\right)^{1/2}$ and ψ is an argument of $z = \eta_1 + \eta_2 i$, i.e., $z = \rho e^{i\psi}$. Putting Eqs [B.2], [B.3], [B.5] and [B.7] together, we obtain the solution to the original boundary-value problem [6].

Practically, the following scheme can be applied. First, a set of Schwarz-Christoffel transformation parameters is selected. Second, we set up a grid on the unit circle to evaluate the Poisson integral [B.7]. Since the integrand can be evaluated at an arbitrary point, we apply a higher-order Gaussian quadrature scheme. It is desirable, however, that the original pre-images of the vertices of the triangle are endpoints of some integration subintervals, rather than interior points. As soon as the quadrature nodes and the coefficients are calculated, the solution [B.7] can be computed at any point inside the unit disk, which then can be mapped onto the triangle. Examples of a grid in the unit disk and the image of this grid in the triangle are presented in **Figure 16**. A grid in polar

coordinates in the unit disk generates a curvilinear grid in the triangle. Note that we generated a grid condensing around the original pre-images of the vertices (Figure 16a) in order to make the grid in the triangle more evenly spaced near the vertices (Figure 16b).

An example of computation of the solution using the transformation [B.1] is presented in **Figure 17**. In Figure 17a, the original pre-image solution in the unit disk is displayed. In Figure 17b, we show the solution of [6] on the triangular domain evaluated at the nodes of the curvilinear grid shown in Figure 16.

4 Acknowledgements

This work was partially supported by the U.S. Department of Energy under Contract No. DE-AC03-76SF00098 and by a gift from Statoil to the UC Oil Consortium at the University of California at Berkeley.

5 References

1. Patzek, T.W., and Kristensen, J. G., *Shape Factor and Hydraulic Conductance in Noncircular Capillaries: II. Two-Phase Creeping Flow.* J. Colloid and Interface Sci, 2001. **JCIS2000-0498**: p. Accepted for print 12/00.
2. Patzek, T.W., *E240- Fundamentals of Multiphase Flow in Porous Media*. First ed. 1999, Berkeley: U.C. Berkeley. 250.
3. Kirkpatrick, S. *Hopping conduction: Experiment versus theory*. in *5th annual Conference on amorphous and Liquid Semiconductors: Proceedings*. 1973. London: Taylor and Francis.

4. Hilfer, R., and Øren, P.E, *Dimensional Analysis of Pore Scale and Field Scale Immiscible Displacement.* Transport in Porous Media, 1996. **22**: p. 53-73.

5. Blunt, M.J., and Sher, H., *Pore Network Modelling of Wetting.* Physical Review E, 1995. **52**(December): p. 6387.

6. Lerdhal, T.R., and Oren, P. E. *SPE 59311, A Predictive Network Model for Three-Phase Flow in Porous Media*. in *SPE/DOE Improved Oil Recovery Symposium*. 2000. Tulsa, OK.

7. Øren, P.-E., Bakke, S., and Arntzen, O. J., *Extending Predictive Capabilities to Network Models.* SPEJ, 1998. **3**(4): p. 324-336.

8. Patzek, T.W. *SPE 59312, Verification of a complete pore network simulator of drainage and imbibition*. in *SPE/DOE Improved Oil Recovery Symposium*. 2000. Tulsa, OK.

9. Hwang, S.-T., *The Gauss Equation of Capillarity.* Zeitschrift für Physikalische Chemie Neue Folge, 1977. **105**: p. 225-235.

10. Mayer, R.P., and Stowe, R. A., *Mercury-Porosimetry Breakthrough Pressure for Penetration between Packed Spheres.* J. Colloid and Interface Science, 1965. **30**: p. 893-911.

11. Princen, H.M., *Capillary Phenomena in Assemblies of Parallel Cylinders. I. Capillary Rise between Two Cylinders.* J. Colloid and Interface Science, 1969. **30**: p. 60.

12. Princen, H.M., *Capillary Phenomena in Assemblies of Parallel Cylinders. II. Capillary Rise in Systems with More than Two Cylinders.* J. Colloid and Interface Science, 1969. **30**: p. 359.

13. Princen, H.M., *Capillary Phenomena in Assemblies of Parallel Cylinders. III. Liquid Columns between Horizontal Parallel Cylinders.* J. Colloid and Interface Science, 1970. **34**: p. 171.

14. Mason, G., and Morrow, N. R., *Capillary Behavior of a Perfectly Wetting Liquid in Irregular Triangular Tubes.* J. Colloid and Interface Science, 1991. **141**: p. 262.

15. Langlois, W.E., *Slow Viscous Flow*. 1964, New York: The Macmillan Company.

16. Bird, R.B., Stewart, W. E., and Lightfoot, E. N., *Transport Phenomena*. 1960, New York: John Wiley & Sons, Inc.

17. Tikhonov, A.N., and Samarskii, A. A., *Equations of mathematical physics*. International series of monographs in pure and applied mathematics; v. 39. 1963, New York: Macmillan.

18. Treefethen, L.N., *Numerical Computation of the Schwarz-Christoffel Transformation.* SIAM J. on Scientific and Statistical Computing, 1980. **1**(1): p. 82-102.

19. Treefethen, L.N., *SPACK User's Guide*, 1989, MIT Numerical Analysis Report 89-2.

20. Driscoll, T.A., *Schwarz-Christoffel Toolbox, Version 2.1*, 1998.

FIGURE CAPTIONS

Figure 1- Corner filament flow is essential; see, e.g., (2).

Figure 2 - Idealization of a pore body and the attached pore throats as cylinders of square and circular cross-sections.

Figure 3 - Basic cross-sections of idealized pore-bodies and pore-throats.

Figure 4 - Triangular pore cross-section.

Figure 5 - The shape factor or "*G*-dome" for triangular pores. The feasible values of the shape factor and the base half-angles are inside the dome. The dome is parameterized by Eq. [A.9]. .

Figure 6 - 1000 realizations of corner half-angles for G=0.03. The horizontal lines in the middle bound β_2.

Figure 7 - Superimposed cross-section outlines for the 1000 realizations in Figure 6.

Figure 8 - Geometry of an equilateral-triangle flow duct.

Figure 9 – Dimensionless hydraulic conductance versus shape factor for random and isosceles triangles from the conformal mapping solutions.

Figure 10 - The dimensionless hydraulic conductance vs. shape factor in one-phase flow in ducts with the triangular (solid line), rectangular (dotted line) and elliptic (dashed line) cross-sections. The stars denote the respective end-point values for equilateral triangle, square and circle. The triangle branch approximates semi-analytical solutions; the rectangle and ellipse branches have been obtained analytically.

Figure 11 - The rectangular cross-section duct.

Figure 12 - The elliptic cross-section duct.

Figure 13 – The rescaled hydraulic conductances vs. rescaled shape factors for the rectangular (dotted line), elliptic (dashed line) and triangular (solid line) cross-section ducts.

Figure 14 - Plot of the cubic polynomial [A.10] at different values of G: G=0 (a); G=0.0241 (b); and G =G_{max} (c)

Figure 15 - Locations of the angles $\varphi_{1,2,3}$ and the roots $t_{1,2,3}$.

Figure 16 – An example of conformal mapping of the unit disk onto a triangle. The polar grid a) is transformed into a curvilinear grid b) in the triangle.

Figure 17 – a) The fluid velocity obtained on the unit disk, and b) its image after mapping [B.1].

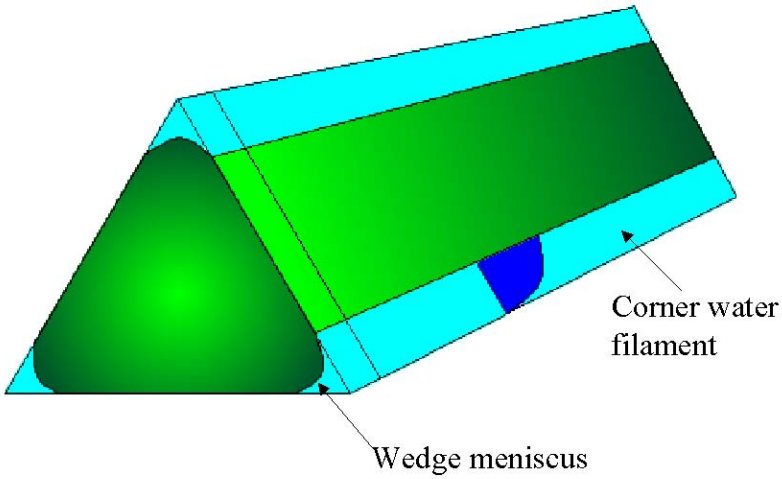

Figure 1

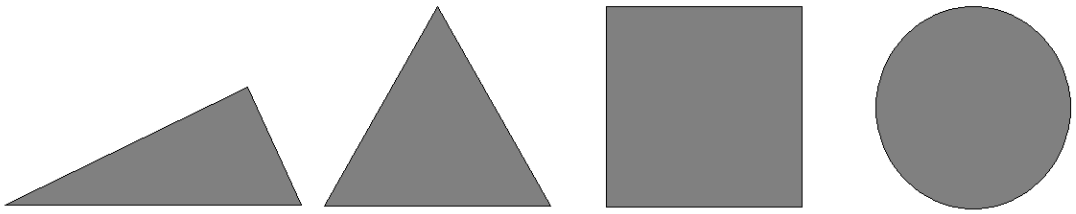

Figure 2

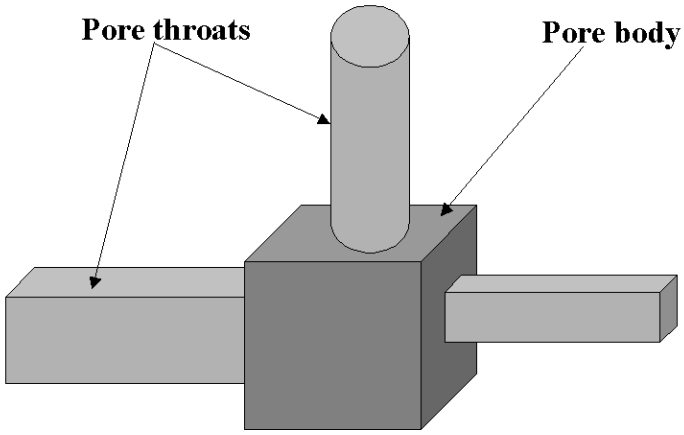

Figure 3

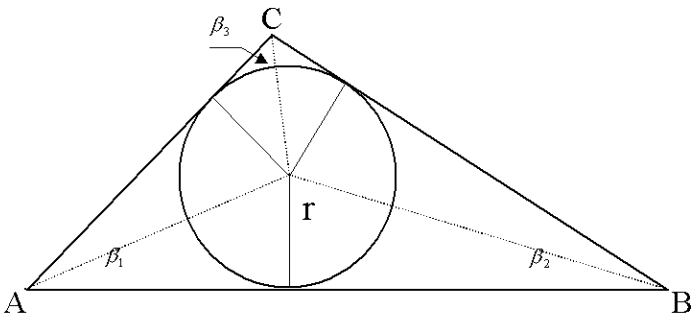

Figure 4

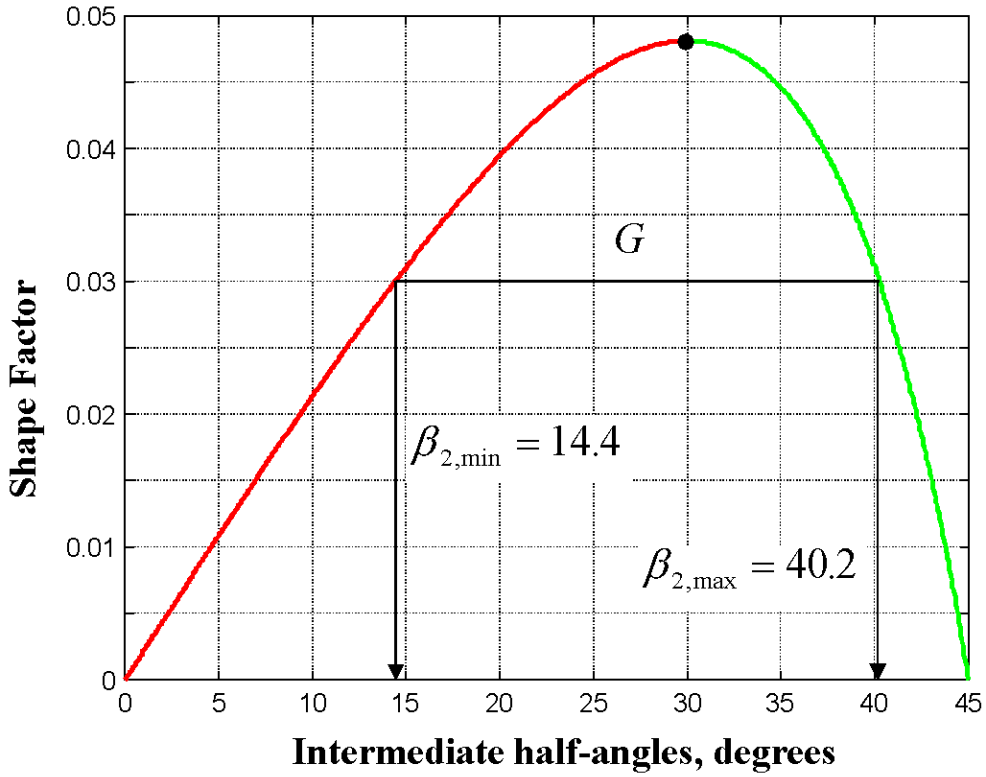
0.05
0.04
0.03
0.02
0.01
0
Shape Factor
G
$\beta_{2,\min} = 14.4$
$\beta_{2,\max} = 40.2$
0
5
10
15
20
25
30
35
40
45
Intermediate half-angles, degrees

Figure 5

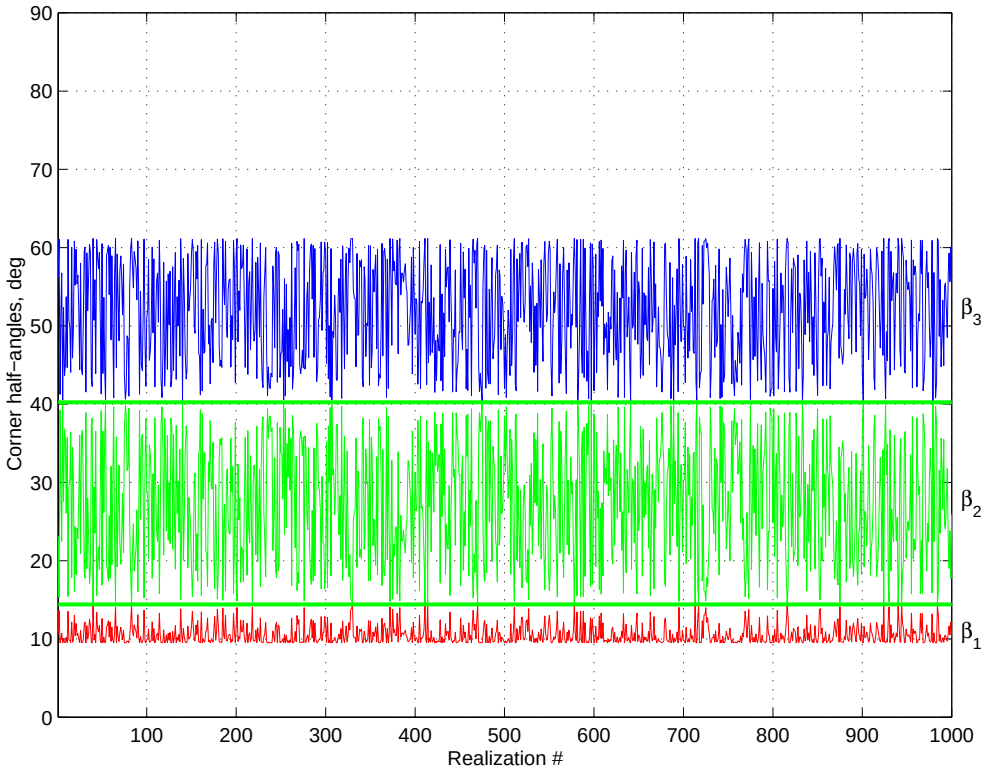
Corner half−angles, deg
Realization #
β3
β2
β1
0
10
20
30
40
50
60
70
80
90
100
200
300
400
500
600
700
800
900
1000

Figure 6

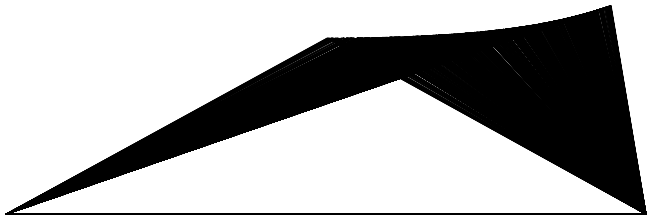

G=0.030, $2\beta_{2,min}$=28.8, $2\beta_{2,max}$=80.5 deg

Figure 7

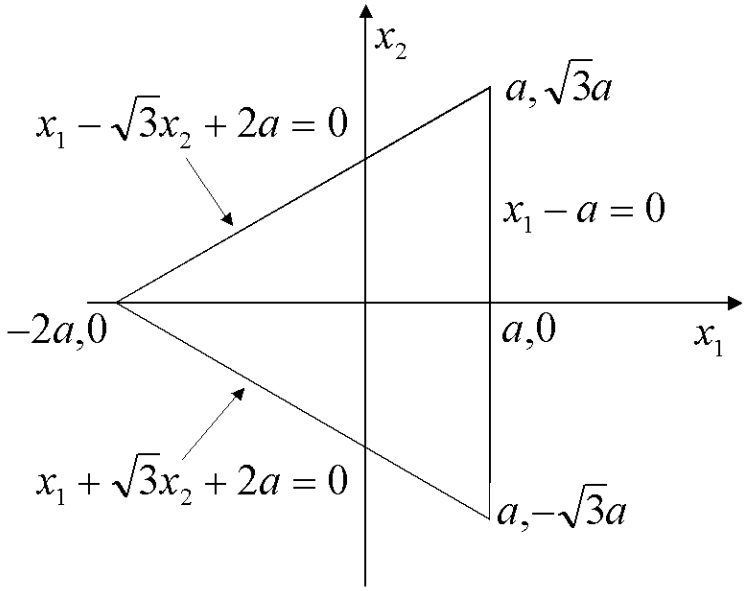
x_2
$a, \sqrt{3}a$
$x_1 - \sqrt{3}x_2 + 2a = 0$
$x_1 - a = 0$
$-2a, 0$
$a, 0$
x_1
$x_1 + \sqrt{3}x_2 + 2a = 0$
$a, -\sqrt{3}a$

Figure 8

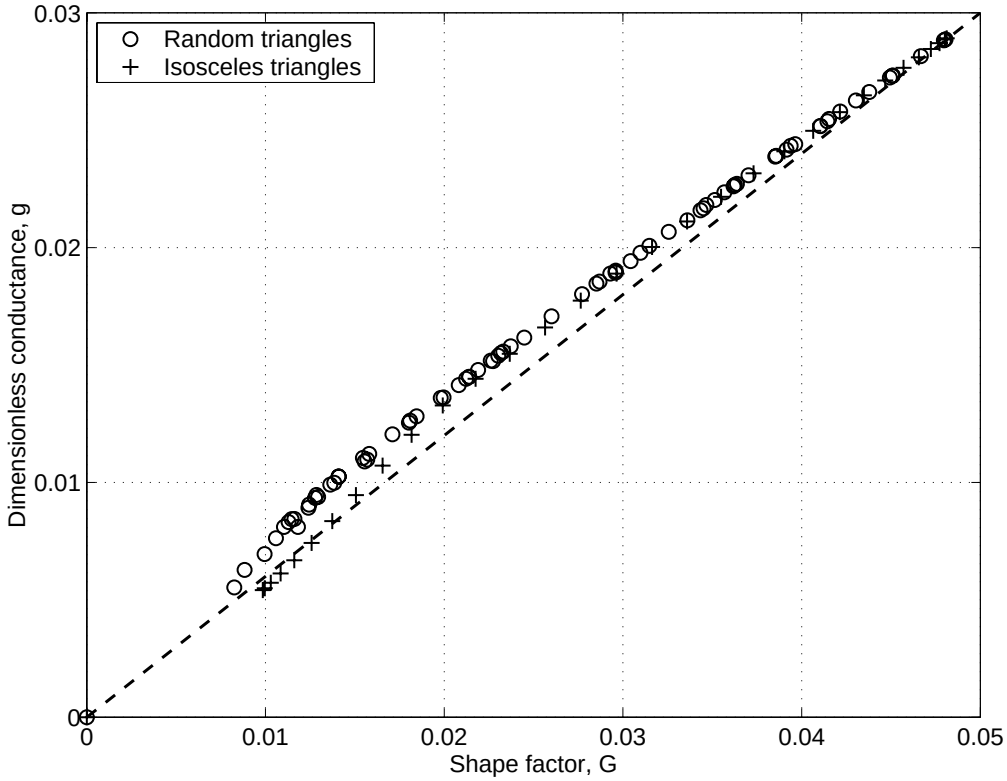
Random triangles
Isosceles triangles
Dimensionless conductance, g
Shape factor, G
0.03
0.02
0.01
0
0
0.01
0.02
0.03
0.04
0.05

Figure 9

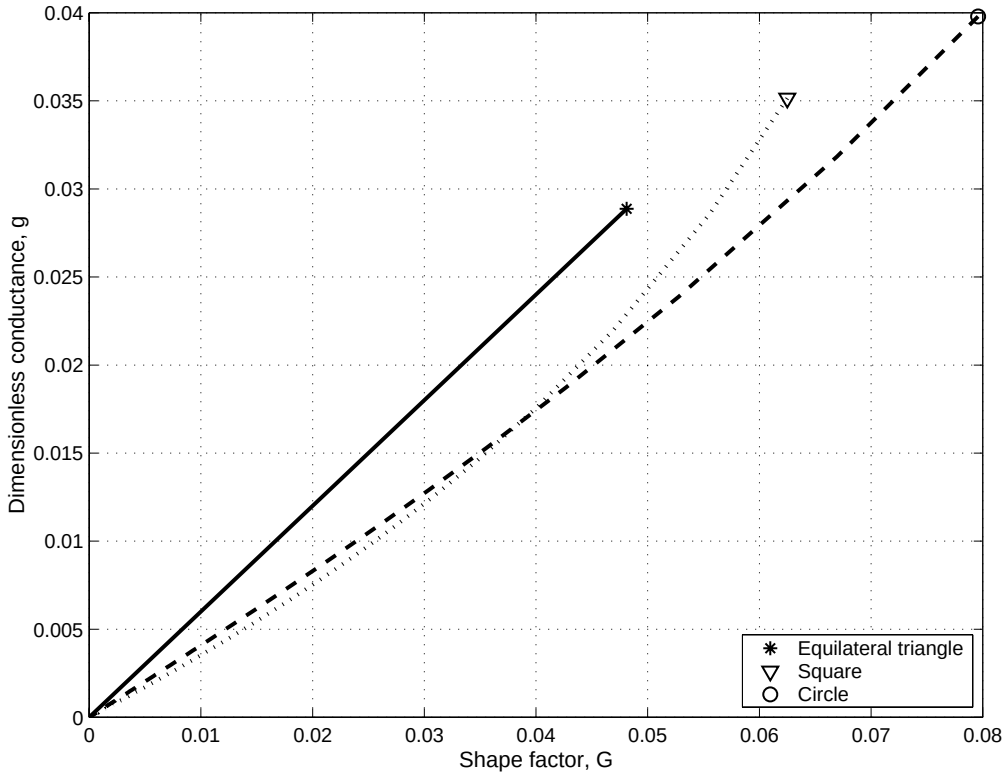
Dimensionless conductance, g
Shape factor, G
0.04
0.035
0.03
0.025
0.02
0.015
0.01
0.005
0
0
0.01
0.02
0.03
0.04
0.05
0.06
0.07
0.08
Equilateral triangle
Square
Circle

Figure

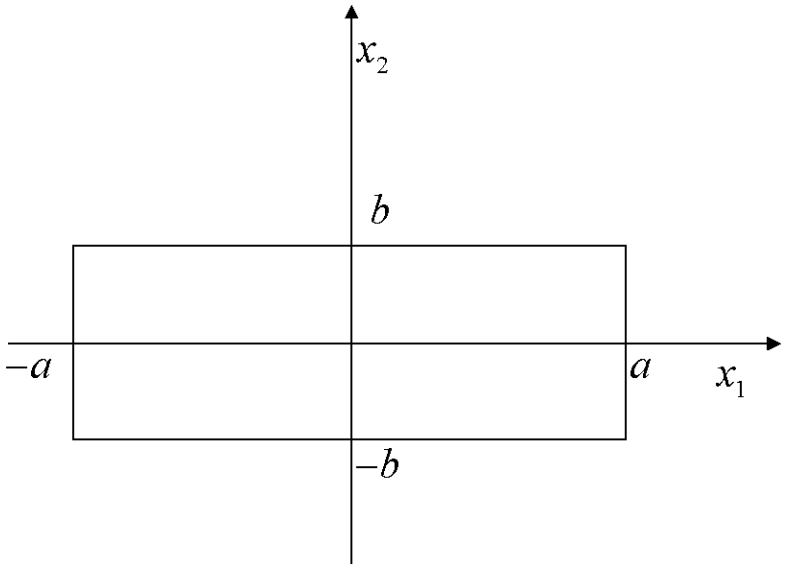

Figure

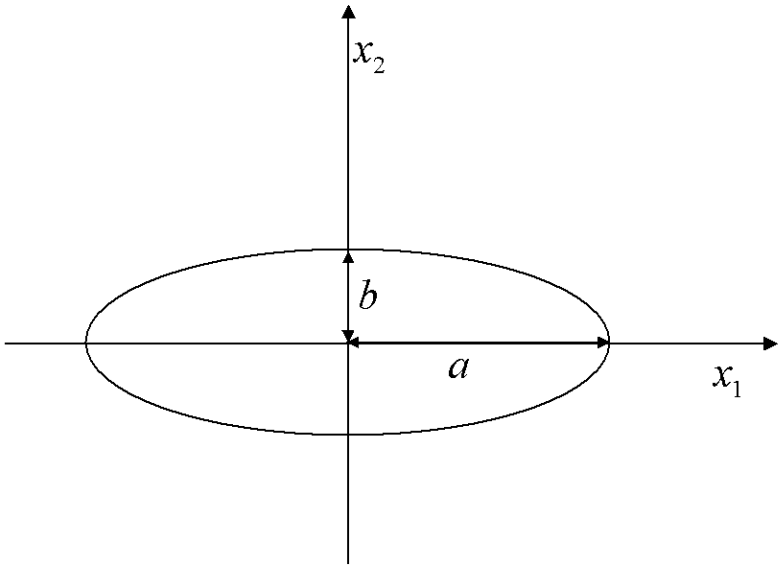
x_2
b
a
x_1

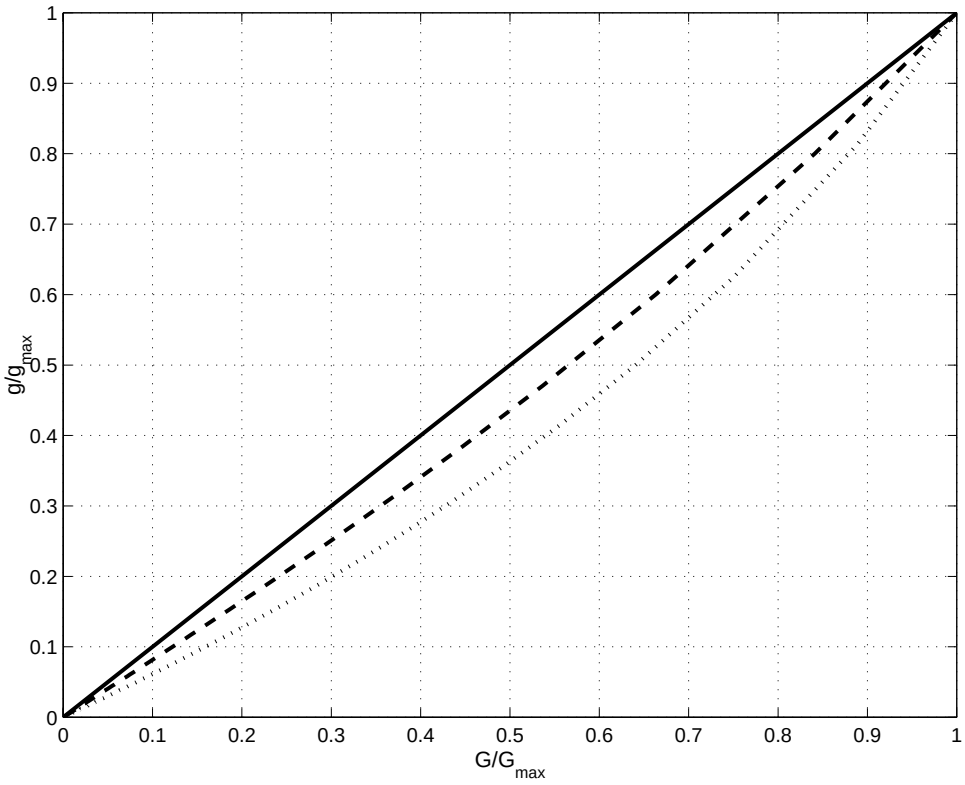

Figure

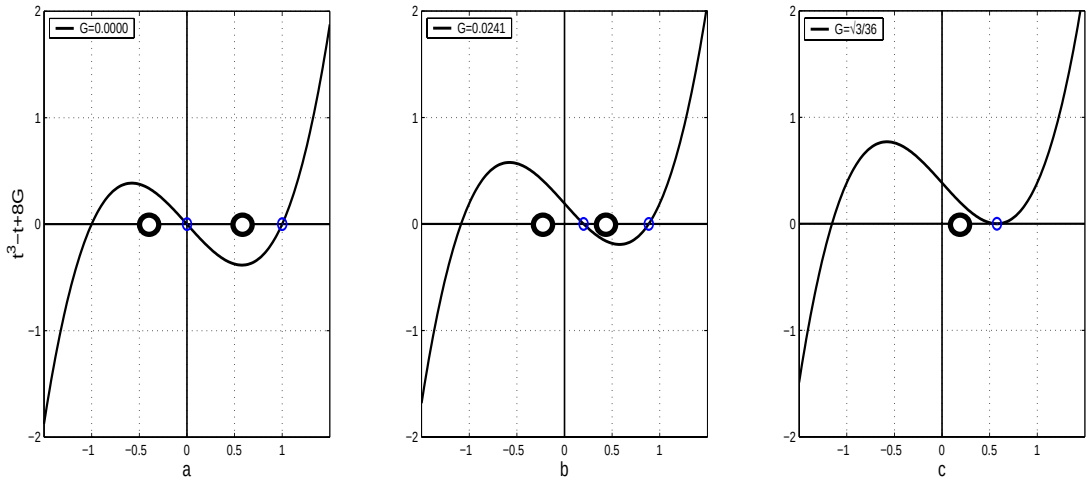

Figure

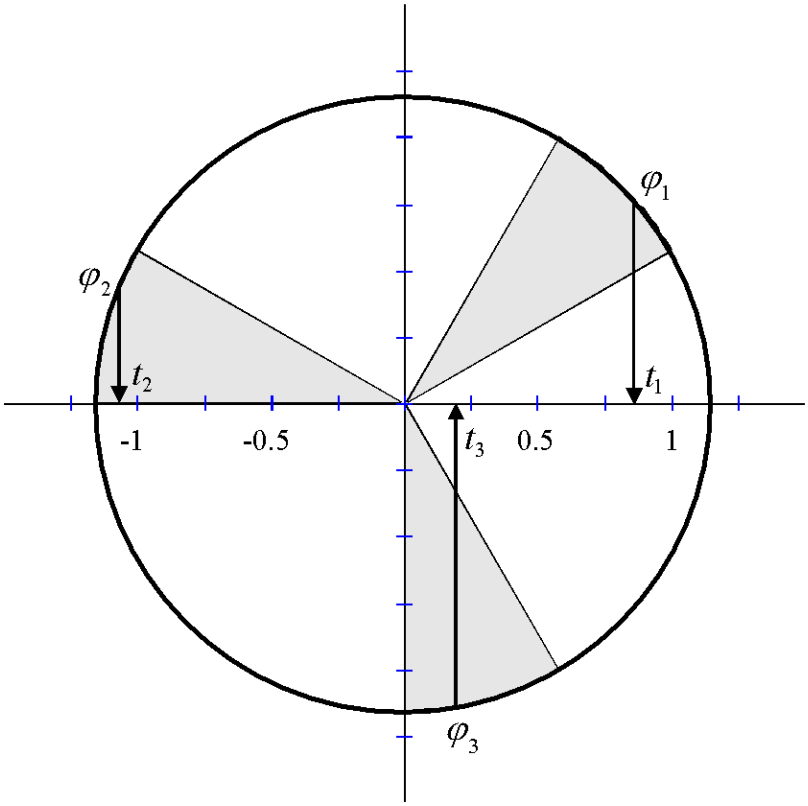
φ_1
φ_2
t_2
t_1
-1
-0.5
t_3
0.5
1
φ_3

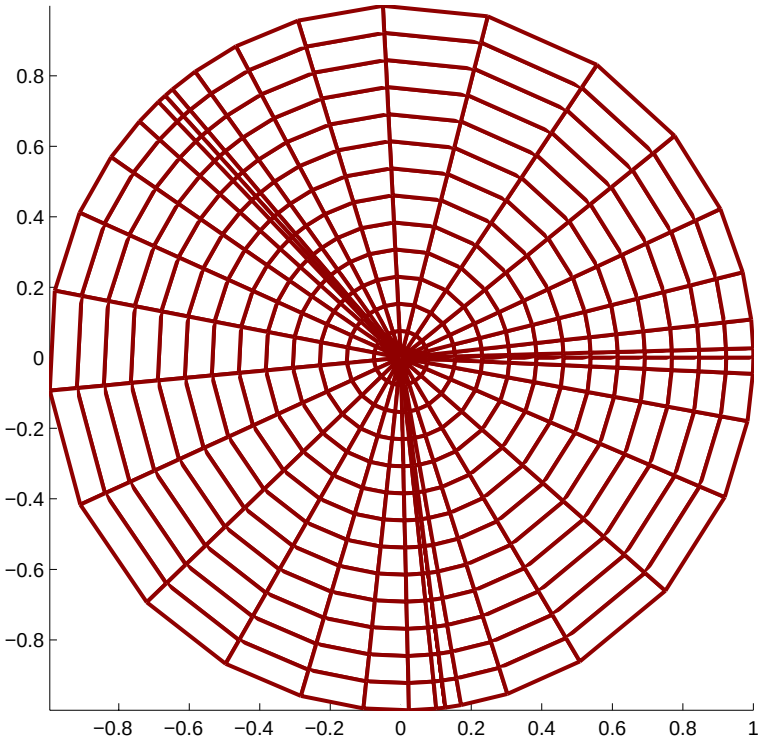

Figure

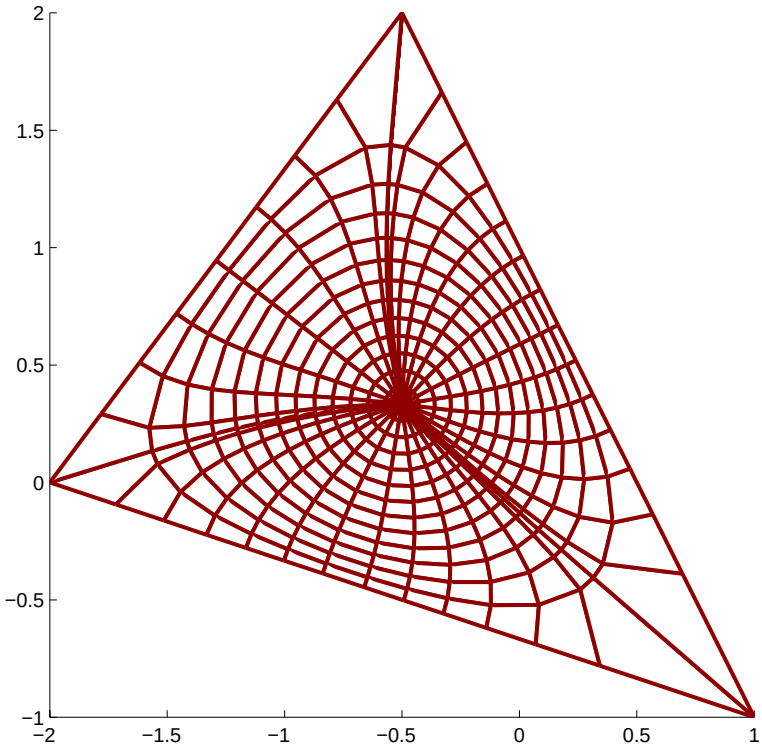

Figure

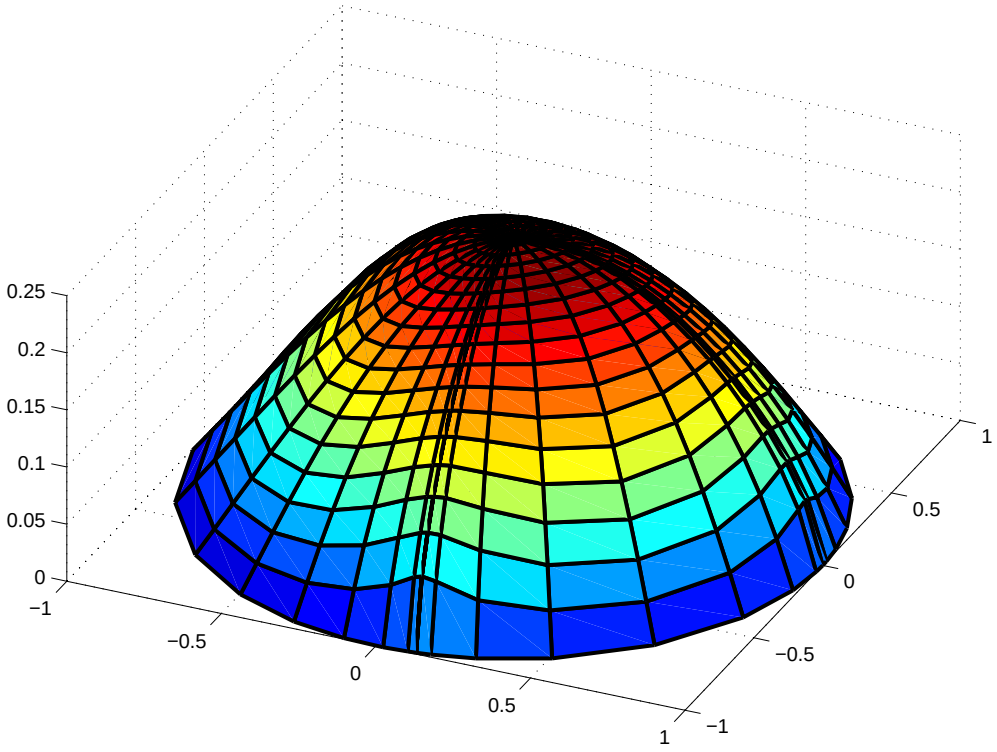

Figure

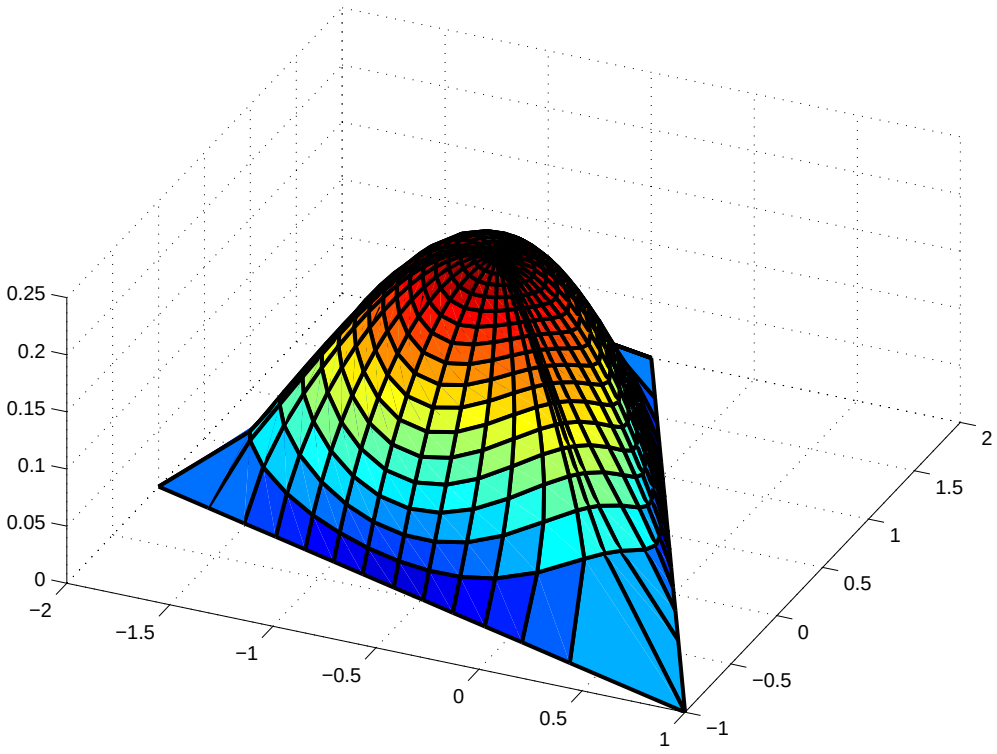

Figure